JGR Oceans

RESEARCH ARTICLE
10.1029/2025JC022463

Key Points:

- Multifractal analysis and spectral kurtosis reveal complex features at nodule point, WA and East River, NY tidal sites
- Spectral kurtosis shows that tidal turbulence intermittency exhibits a unique pattern distinct from grid and wall-bounded turbulence
- Multifractal analysis reveals higher Hurst exponents in ebb flows and greater multifractality in flood flows at nodule point

Correspondence to:
V. S. Neary and L. P. Chamorro,
vsneary@sandia.gov;
lpchamo@illinois.edu

Citation:
Cheng, S., Neary, V. S., & Chamorro, L. P. (2025). Directional variations in tidal flow multifractality and intermittency. *Journal of Geophysical Research: Oceans*, *130*, e2025JC022463. https://doi.org/10.1029/2025JC022463

Received 10 FEB 2025
Accepted 18 MAY 2025

Author Contributions:
Conceptualization: Shyuan Cheng, Vincent S. Neary, Leonardo P. Chamorro
Data curation: Shyuan Cheng
Formal analysis: Shyuan Cheng
Funding acquisition: Vincent S. Neary, Leonardo P. Chamorro
Investigation: Leonardo P. Chamorro
Methodology: Shyuan Cheng
Project administration: Vincent S. Neary
Resources: Vincent S. Neary
Supervision: Leonardo P. Chamorro
Writing – original draft: Shyuan Cheng
Writing – review & editing: Vincent S. Neary, Leonardo P. Chamorro

Directional Variations in Tidal Flow Multifractality and Intermittency

Shyuan Cheng[1], **Vincent S. Neary**[2], **and Leonardo P. Chamorro**[1,3,4,5]

[1]Mechanical Science and Engineering, University of Illinois Urbana-Champaign, Urbana, IL, USA, [2]Sandia National Laboratories, Albuquerque, NM, USA, [3]Civil and Environmental Engineering, University of Illinois Urbana-Champaign, Urbana, IL, USA, [4]Aerospace Engineering, University of Illinois Urbana-Champaign, Urbana, IL, USA, [5]Geology, University of Illinois Urbana-Champaign, Urbana, IL, USA

Abstract We explored distinct directional variations of multifractal and intermittent characteristics of ebb and flood flow velocities at nodule point, WA, tidal energy site, and complementary inspection on the East River, NY using scaling exponents of the structure function, distribution flatness, detrending moving average (DMA) analysis, multifractal detrended fluctuation analysis (MF-DFA), and high-order spectral moments. Our findings reveal that tidal flow presents higher long-range dependence (LRD) and intermittent levels for the ebb flow sections, whereas the flood flow sections exhibit a higher degree of multifractality and greater sensitivity to larger magnitude of turbulent fluctuations. We demonstrate that long-range dependence predominantly contributes to multifractal behavior in both ebb and flood flows, as evidenced by the significantly reduced multifractal spectrum width for temporally randomly permuted time series. Moreover, spectral kurtosis analysis uncovers a higher intermittent level across all frequency scales for ebb flow sections and reveals a distinct pattern of tidal flow intermittency differing from the monotonically increasing intermittent level observed in wall-bounded and grid turbulence. Finally, we demonstrate that DMA, MF-DFA, and high-order spectral moments provide more comprehensive insights than structure function scaling exponents and PDF flatness methods.

Plain Language Summary Tidal currents plays an important role in marine ecosystems, sediment transport, and renewable energy. However, their complex dynamics, influenced by turbulence and intermittency, remain poorly understood. We used multifractal detrended fluctuation analysis (MF-DFA) and spectral kurtosis to investigate tidal flows at nodule point, WA, and East River, NY, uncovering distinct directional variations in their multifractal and intermittency characteristics, where its ebb flow showed higher long-range dependence (LRD), whereas the flood flow exhibited greater multifractality and susceptibility to large magnitude of turbulent fluctuations. By employing higher-order spectral analysis and detrending techniques to isolate short-term dynamics, the study reveals unique scale-dependent intermittency patterns in tidal turbulence. For the first time, a characteristic tidal intermittency pattern is observed, featuring higher intermittency levels at midinertial subrange scales and Gaussian-like behavior in small-scale events, which distinct from classical grid turbulence models. These findings advance the understanding of tidal turbulence patterns by incorporating multifractal dynamics, offering new insights for the design and placement of tidal turbines to optimize energy extraction. The results align with prior efforts and highlight the value of integrating multifractal analysis into models to enhance our understanding and utilization of tidal systems.

1. Introduction

Over the last decade, tidal stream energy has demonstrated the reliability of tidal energy conversion (TEC) technologies through real-world deployments. These demonstrations show the potential of tidal energy to enhance the global renewable energy mix. This includes utility-scale grid-connected tidal energy projects as well as off-grid or distributed systems serving coastal and island communities. Such initiatives offer solutions to meet the diverse energy needs of these communities particularly those that are off-grid (Chowdhury et al., 2021; Huckerby et al., 2016; OES, 2023). The maximum extractable global mean annual tidal power along continental shelves is estimated to be a fraction of the 2.5 TW (TW) dissipation rate (Egbert & Ray, 2003), ranging from 0.06 TW (Hammons, 1993) to 1 TW (Kempener & Neumann, 2014). This indicates that fully harnessing global tidal current energy could significantly contribute to the projected 2050 global mean annual renewable power electricity generation of 4.8 TW (EIA, 2023).

As tidal energy deployment scales up, employing simulators to perform life cycle analysis of hydrokinetic turbines becomes necessary to estimate the levelized costs of energy (LCOE) for tidal site selection. One of the most commonly used approaches is the TurbSim stochastic unsteady turbulent inflow simulator developed by the National Renewable Energy Laboratory (NREL) (Kelley & Jonkman, 2005). TurbSim is an inflow wind/tidal-based simulation tool that offers a variety of turbulence spectrum models, such as the IEC Kaimal Model and the IEC von Kármán Isotropic Model. It inputs single-point mean flow speed, turbulence intensity, and integral length/timescales obtained from field measurements and returns a velocity time series by inverse Fourier transforming the turbulence spectrum representation (Jonkman, 2009). These simulated time series of velocity fluctuations are utilized for turbine load analysis, imbalance fault diagnosis, and LCOE estimation (Bashirzadeh Tabrizi et al., 2019; Malik & Mishra, 2017). Despite TurbSim's effectiveness in aiding turbine design, installation, operation, and maintenance processes (Byon, 2013; El-Thalji & Liyanage, 2012; Foley & Gutowski, 2008), the linear nature of classical spectrum models adopted in TurbSim introduces several limitations, including the omission of turbulence intermittency and the inability to model multifractal characteristics in the flow (Kelty-Stephen et al., 2023).

Intermittency in turbulence significantly affects tidal and wind turbines. Anup et al. (2021) experimentally demonstrated that small-scale intermittent structures lead to increased turbine loading. Their findings also included heavy-tailed distributions in rotor torque and blade bending moment under more intermittent wind conditions. Ali and Cal (2019) conducted experimental research on the near wake of a wind turbine array, uncovering its multifractal characteristics through the second-order structure function and multifractal detrended fluctuation analysis. They observed high intermittency at various scales within the turbine array wake potentially linked to rotor blade vibration modes. Milan et al. (2013) used multifractal analysis on wind farm power output data, employing scaling exponents of structure functions and the flatness of PDF distributions. They identified that the fractal scaling of the highly fluctuating electrical power produced by wind turbines closely aligns with Kolmogorov's log-normal law of turbulence, attributing the fluctuations to highly intermittent wind gusts. Their analysis further showed that wind turbines amplify the level of intermittency by up to four times that of the incoming wind, a characteristic also evident in wind farms where the cumulative farm power significantly deviates from a Gaussian distribution.

Tidal flood and ebb flows exhibit distinct characteristics with their asymmetry influenced by bathymetry, channel geometry, tidal forcing, and external environmental factors and demonstrate the complex interplay of physical and environmental factors that shape tidal asymmetries, with implications for sediment transport, nutrient cycling, flood risk management and tidal energy extraction. In general, flood flows show stronger peak velocities and shorter durations, whereas ebb flows tend to have weaker velocities and longer durations particularly in regions with tidal distortion (Dronkers, 1986; Jay & Musiak, 1994).

Burchard and Baumert (1998) demonstrated that stratification and vertical mixing caused by tidal currents significantly alter flood-ebb flow differences particularly in estuaries with strong freshwater input. Dronkers (1986) highlighted the influence of channel convergence on flood dominance, where narrower channels amplify tidal flood velocities. Field measurements using Acoustic Doppler current profilers by Fong et al. (2009) highlight the asymmetry in Reynolds stress over tidal cycles and discuss the challenges in simulating these flows. Nepf and Geyer (1996) explored intratidal variations in a narrow section of the Hudson River and noted differences in mixing between flood and ebb tides. In particular, they noted that active mixing is largely confined to a near-bed layer during flood with significant stratification in ebb. MacDonald and Horner-Devine (2008) explored the spatiotemporal variability of vertical salt flux in the Fraser River Estuary, British Columbia. They found that vertical salt flux served as the primary mechanism for salt removal during tidal cycles with ebb tides displaying 2 to 3 times greater flux compared to floods. This disparity was attributed to increased vertical shear of horizontal velocity and enhanced mixing in regions characterized by channel constriction. Brown and Davies (2010) examined flood/ebb tidal dominance and its effect on estuarine sediment transport using the Dyfi Estuary, UK. Observations suggest ebb dominance, leading to net sand transport out of the estuary, whereas flood dominance in the upper estuary results in up-estuary transport primarily influenced by channel and sandflat distribution. Laboratory experiments by Geng et al. (2020) explored the differential impacts of flood and ebb currents on tidal channel network formation using a sloping tidal-flat basin model. Findings demonstrate that ebb currents, intensified by a slight incline that diminishes flood current energy, are more effective at initiating and developing complex, deeper tidal networks. Conversely, flood-dominated tides typically form smaller more branched channels in the upper basin.

Long-range temporal persistence in tidal, riverine, and wind turbulence was first observed by Hurst (1951), who introduced the Hurst exponent H to quantify the extent of temporal long-range dependence. Following Hurst's pioneering work, the phenomena of Hurst persistence in various geophysical time series and atmospheric boundary layer data have been extensively investigated (Dike & Agunwamba, 2012; Hurst, 1951; Lumley, 1981; Mandelbrot & Wallis, 1968). Recent studies have shown that geophysical processes typically display scale-dependent features and are multifractal (Adarsh et al., 2020; Li et al., 2015; Wu et al., 2018; Zhang et al., 2009), indicating that classical statistical theories of turbulence may be inadequate to fully characterize these geophysical processes and prompt for multifractal analysis. However, the spectrum in TurbSim does not capture the Hurst effect and the multifractal characteristics constrained by the linear spectrum models.

The linear classical spectrum models presuppose symmetry over time with stable mean, variance, and autocorrelation (Kelty-Stephen et al., 2023). Dias et al. (2018) explored atmospheric turbulence and demonstrated that a persistence process (i.e., $H > 0.5$) indicates the absence of a statistically significant integral timescale, indicating the inaccuracy of velocity time series simulated by classical turbulence spectrum models. Indeed, the von Kármán and Kaimal models can only return a flat spectrum in the energy-containing range because they assume past processes are independent and do not influence later autocorrelation. This leads to a significant underestimation of the energy-containing range power spectra density of tidal flow as shown by Cheng et al. (2024) (refer to their Figure 15c). Recently, Laudani et al. (2021) introduced two novel spectrum models that incorporate fractal dimension and Hurst effect through a robust correlation structure using generalized Cauchy and Dagum models. Their models surpass the widely adopted von Kármán and Kaimal models in atmospheric boundary layer spectrum modeling, showing less discrepancy between field-measured spectra across the energy-containing and inertial subranges. These results highlight the strong interaction between wind/tidal currents and turbines, indicating that tidal turbulence significantly affects the fatigue load on turbines (Bossuyt et al., 2016) and cause large fluctuations in power grids (Milan et al., 2013; Tarroja et al., 2011). There is a need to characterize the intermittent effects and multifractal characteristics that can be incorporated into future turbulence modeling.

Here, we compare various multifractality and intermittency estimation methods, including the scaling exponents of the structure function, distribution flatness, detrending moving average (DMA) analysis, multifractal detrended fluctuation analysis (MF-DFA), and high-order spectral moments. Also, using the EMD-detrend technique, we demonstrate how the scale-dependent intermittent behavior of nonstationary tidal velocity time series can be characterized. The Hurst exponent H and intermittent component c_1, obtained via traditional structure function scaling exponents, are compared with the generalized Hurst exponent H_q estimated by detrending moving average (DMA) and multifractal detrended fluctuation analysis (MF-DFA). Also, scale-dependent intermittent levels are obtained using high-order spectral moments proposed by Lortie and Mydlarski (2022), which are then compared with the flatness of velocity probability density function (PDF) distributions.

This framework is applied to field-measured velocity time series from tidal energy sites to investigate the scale-invariant multifractal and intermittent properties across different sections of the flood and ebb flows. The flood and ebb flow sections exhibit distinct dynamics influenced by regional and site characteristics and geophysical interference, displaying self-affine fractal behaviors across multiple timescales. These characteristics have implications for marine turbine inflow condition (Adarsh et al., 2020). The paper is organized as follows: Section 2 introduces the tidal energy sites, Section 3 outlines the methods of analysis, Section 4 provides detailed results of structure functions, multifractal analysis, and intermittency analysis, discussion is provided in Section 5, and main remarks are included in Section 6.

2. Tidal Current Data

We examined the multifractal and intermittent properties in two tidal sites: nodule point, WA, and East River, NY. The first data set was obtained from a single ping Nortek Vector Acoustic Doppler Velocimeter (ADV) operated at 6 MHz during the spring tide from 17 February to 21 February 2011 with a sampling frequency of $f_s = 32$ Hz over one hundred hours (4.3 days). The ADV was positioned at the apex of the Tidal Turbulence Tripod, which was located 4.7 m above the seabed that was 22 m deep at nodule point, located on the eastern side of Marrowstone Island (Figure 1a). For more information on the sampling parameters and Doppler noise, refer to Thomson et al. (2012), where the need for accurate turbulence intensity measurements is discussed in the context of predicting fatigue and optimizing tidal turbine design. By focusing on turbulence scales relevant to turbine components, it may be possible to lower damage equivalent loads (DELs) and reduce costs.

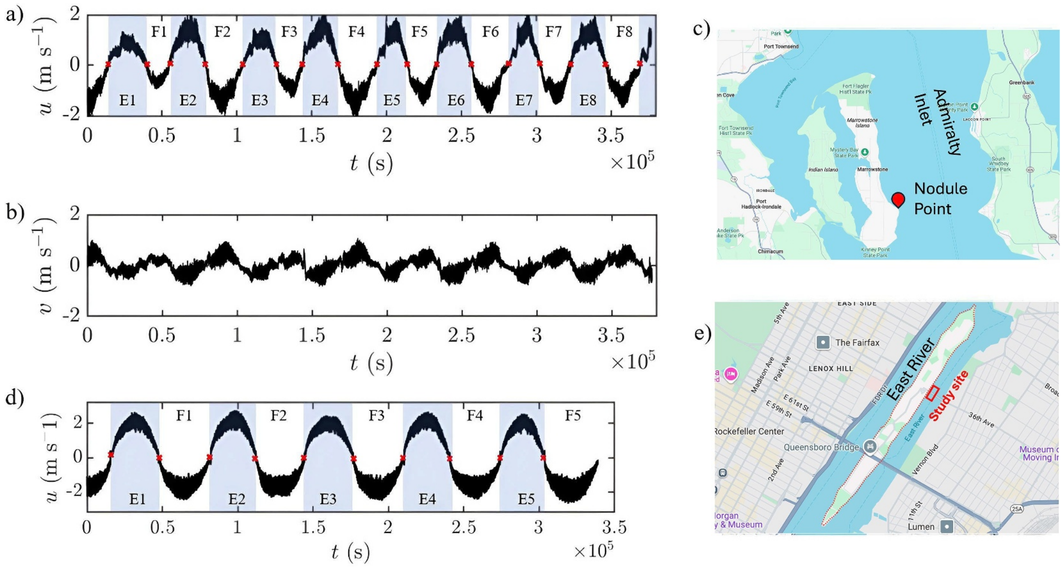

Figure 1. (a, b, c) Velocity time series from nodule point, WA. (a) Streamwise velocity u, (b) spanwise velocity v, and (c) regional map showing the nodule point location. (d, e) Velocity time series from East River, NY. (d) Streamwise velocity u and (e) regional map showing study site location. The blue color region in (a, d) illustrates positive velocities during ebb flow sections and the white color regions indicate negative velocities during flood flow sections.

The second data set was collected using an ADV for a duration of 39 days between 09 June to 17 July 2011 with a sampling frequency of $f_s = 20$ Hz. The upward-looking Sontek Flow Tracker ADV was deployed at the Roosevelt Island Tidal Energy (RITE) site, owned by Verdant Power. The RITE Project site is located on the east side of Roosevelt Island between the boroughs of Manhattan and Queens, New York City. For details on the site characteristics, refer to Gunawan et al. (2014).

These two sites were specifically selected for their strong potential in tidal energy development. As a step toward improving the estimation of the levelized cost of energy (LCOE) for tidal projects, we aim to expand upon the basic tidal flow characterizations presented by Thomson et al. (2012) and Gunawan et al. (2014) by incorporating Hurst and intermittency effects using the same data set to enable direct comparison.

3. Methodology

We investigated tidal flows in both ebb and flood directions, selecting eight distinct time intervals identified by zero-velocity crossing points within the streamwise velocity time series of tidal flows as illustrated in Figure 1. Each section of the velocity time series was subsequently detrended employing an empirical mode decomposition (EMD)-based method (Cheng et al., 2024), resulting in a wide-sense stationary time series of streamwise velocity fluctuations normalized to a zero mean (see the noise-like time series x_k in Figure 2g as the detrended time series for the first ebb section). This facilitates further linear and nonlinear statistical analysis, enabling the characterization of unique intermittent and multifractal features present in both ebb and flood tidal flows.

3.1. Higher Order Spectral Moments—Intermittency

Spectral-based tools are commonly used to detect bursts or transient events in fault detection of rolling machines and bearings (Antoni & Randall, 2006; Hu et al., 2019). Higher-order spectral moments are also used for analyzing acoustic signals affected by under-ice noise, which remain undetectable by power spectral densities owing to their highly impulsive and transient characteristics. Dwyer (1983) used the real and imaginary parts of the complex third- and fourth-order normalized moments (i.e., the spectral skewness and kurtosis) to identify transients of under-ice noise in the frequency domain. Based on this, Pagnan et al. (1994) later proposed the use of the magnitude of the complex fourth-order moment to obtain a more complete picture of the transients present in a signal. Antoni and Randall (2006) undertook a rigorous derivation of the properties of the spectral kurtosis, demonstrating that this higher-order moment is particularly well-suited for the detection of transients in a signal.

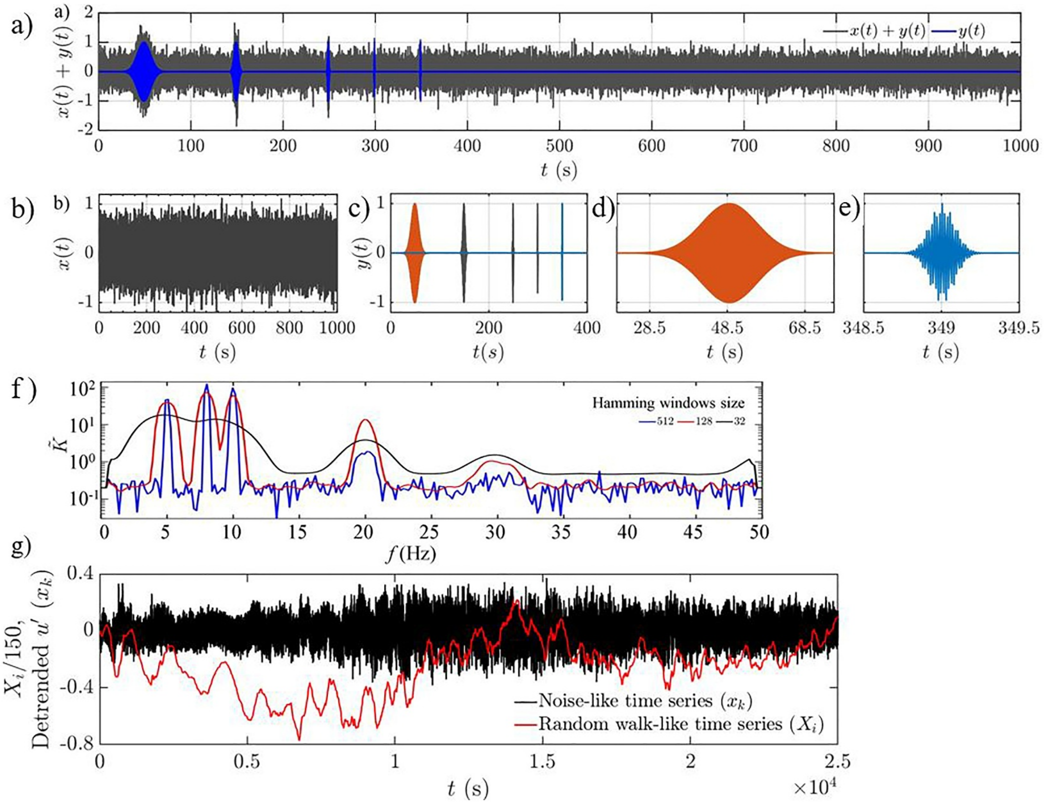

Figure 2. (a) Time series sample combining Gaussian white noise $x(t)$ with five transient events $y(t)$. (b) Gaussian white noise time series $x(t)$. (c) Transient events $y(t)$ featuring various durations and frequencies. (d) Close-up of a transient event lasting approximately 40 s. (e) Detail of a transient event with a duration of approximately 0.5 s. (f) Spectral kurtosis evaluated with different filtering window lengths: 32 (black), 128 (red), and 512 (blue) samples. (g) Detrended velocity fluctuation time series illustrating a noise-like structure alongside the corresponding random walk-like time series generated using Equation 6.

For a time series $x(t)$ sampled at a frequency of f_s, the Welch method is used to separate the entire signal into M segments of length N to compute the short-time Fourier transform, where

$$x(t) = x\big([n + N(m-1)]/f_s\big), n = 0, \ldots, N-1,\ m = 1, \ldots, M. \tag{1}$$

The discrete Fourier transform of each segment is computed as:

$$X(\omega_n, m) = \sum_{k=0}^{N-1} x(k,m)e^{jkn/N}, \tag{2}$$

where $\omega_n = s\pi n f_s/N$ and $j = \sqrt{-1}$.

The Short-time Fourier Transform (STFT) is applied to calculate the discrete Fourier transform (DFT) for each segment of the time series. To mitigate spectral leakage, a filtering window, w_k, is used, resulting in the DFT of each segment being defined as follows:

$$X(\omega_n, m) = \sum_{k=0}^{N-1} w(k)x(k,m)e^{jkn/N}, \tag{3}$$

Hamming window of 75% overlap is selected to divide the full-time series into STFT segments to avoid the stationary data out-dominate the transient event (Lortie & Mydlarski, 2022).

The spectral skewness, $\tilde{S}$, and spectral kurtosis, $\tilde{K}$, are defined as the third- and forth-order moments of the frequency-domain PDFs obtained from the short-time Fourier transform and given as follows:

$$\tilde{S}(\omega_n) = \frac{\frac{1}{M}\sum_{m=1}^{M} |X(\omega_n, m)|^3}{\left(\frac{1}{M}\sum_{m=1}^{M} |X(\omega_n, m)|^2\right)^{3/2}},\ \tilde{K}(\omega_n) = \frac{\frac{1}{M}\sum_{m=1}^{M} |X(\omega_n, m)|^4}{\left(\frac{1}{M}\sum_{m=1}^{M} |X(\omega_n, m)|^2\right)^{2}}. \tag{4}$$

The ability to use the high-order spectral moment to detect transients is demonstrated using a sample signal, consisting of a Gaussian white noise $x(t)$ sampled at 100 Hz and transients $y(t)$ of varying duration and frequency that appear at different time instants. The signals $x(t)$ and $y(t)$ are shown in Figures 2b and 2c, and $y(t)$ is defined as follows:

$$y(t) = A\cos(2\pi f t)e^{\lambda(t-\tau)^2}. \tag{5}$$

Here, A controls the amplitude, f is the characteristic frequency of the transients set as $f = 5$, 8, 10, 20 and 30 Hz, and λ and τ control the transient duration (i.e., signal decay rate) and temporal offset.

Figure 2f shows the spectral Kurtosis $\tilde{K}$ onto sample signal $x(t) + y(t)$ using various Hamming filtering window sizes in STFT. This highlights the ability of using higher-order spectral moments to detect short, intermittent behavior within a time series even when the transients have a magnitude similar to the white-noise signal (Figure 2a), which cannot be detected by typical spectrum analysis and PDF flatness. Figure 2f also shows how STFT window size affects spectral Kurtosis results, namely that a window size much larger than transient duration is dominated by the white noise and the $\tilde{K}$ magnitude decreases (refer to the 30 Hz transient for window size 512 case). The small window size suffers from poor frequency domain resolution and fails to capture low-frequency transients (see $f \leq 15$ Hz result for window size = 32 samples), highlighting the importance of STFT parameter selection in computing high-order spectral moments.

3.2. Long-Range Dependence

Two methods are used here to evaluate the long-range dependence (LRD) of the time series, the detrending moving average and multifractal detrended fluctuations analysis, which are described as follows.

3.2.1. Detrending Moving Average Analysis (DMA)

The detrending moving average (DMA) is a simple yet effective method for examining the scaling characteristics of the local standard deviation around a moving average. The application of DMA to a time series x_k with length N involves the following procedures. First, a random walk-like time series profile is generated from the noise-like detrended time series x_k by integrating the time series with mean subtracted (Figure 2g) as follows:

$$X_i = \sum_{k=1}^{i}(x_k - \langle x_k \rangle), \quad i = 1, \dots, N. \tag{6}$$

Then, the moving average $\bar{X}_n(t)$ of the random walk-like signal X_i is computed over a range of moving time windows of length n, given by:

$$\bar{X}_n(t) = \frac{1}{n}\sum_{k=t-n+1}^{t} X_k, \tag{7}$$

where t ranges from n to N. Finally, the standard deviation of the detrended signal is calculated by subtracting the moving average function $\bar{X}_n(t)$ from the original series X_i leading to σ^2_{DMA}, which is the variance as a function of window size n, given by:

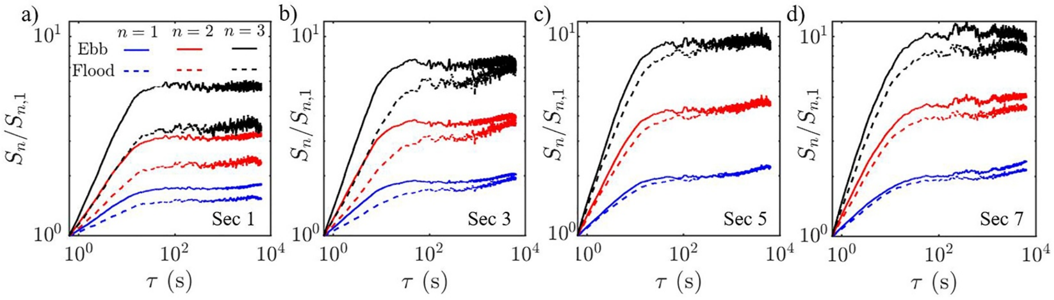

Figure 3. Selected sections of n-th order structure functions for various ebb flows (solid lines) and flood flows (dashed lines): (a) Section 1, (b) Section 3, (c) Section 5, and (d) Section 7 (Figure 1), with S_1, S_2, and S_3 represented in blue, red, and black.

$$\sigma_{DMA}^2 = \frac{1}{N-n+1}\sum_{t=n}^{N}\left[X_t - \bar{X}_n(t)\right]^2. \tag{8}$$

After obtaining the standard deviation $\sigma_{DMA,n}(t)$, the Hurst exponent is expected to behave as $\sigma_n(t) \sim n^H$ and can be estimated by a “linear” fit in the log-log representation of the standard deviation σ_n versus moving average window size n.

3.3. Multifractal Detrended Fluctuation Analysis (MF-DFA)

The type of time series under inspection is often subjected to nonstationarities, including artificial noises and trends, which may lead to unreliable or even spurious results in data analysis. Multifractal detrended fluctuation analysis (MF-DFA) is extensively used to investigate the multifractal properties and scaling behaviors of nonstationary time series. The first step in MF-DFA is identical to step one of DMA, involving the generation of a random walk signal from the noise-like time series x_k as shown in Figure 2g. Following this, the random walk-like profile X_i is divided into nonoverlapping intervals $N_s = \text{int}(N/s)$ with equal timescale s. Subsequently, a local trend for N_s segments is determined using a least squares fit method. The variance for each segment $v = 1, \ldots, N_s$, where $x_v(i)$ and $y_v(i)$ represent the fitting polynomial in the v-th segment, is defined as:

$$F^2(s,v) = \frac{1}{s}\sum_{i=1}^{s}\{X[(v-1)s+i] - x_v(i)\}^2. \tag{9}$$

A third-order polynomial is typically used in the fitting process. The next step involves averaging the qth-order fluctuation function, $F_q(s)$, over all segments expressed as

$$F_q(s) = \left\{\frac{1}{N_S}\sum_{v=1}^{N_s}\left[F^2(s,v)\right]^{q/2}\right\}^{1/q}, \text{for } q \neq 0. \tag{10}$$

Finally, the slope of the log-log representation of $F_q(s)$ versus s is calculated. The generalized Hurst exponent $H_q(q)$, used for multifractal analysis, is taken as the scaling exponent, described by $F_q(s) \sim s^{H_q(q)}$, where $H_q(q = 2)$ represents the original Hurst exponent for monofractal analysis.

4. Nodule Point, WA Tidal Site Results

4.1. Structure Functions

We examine various orders, n, of structure functions defined as $S_n(\tau) = \langle |u(t+\tau) - u(t)|^n \rangle$, where τ is the time lag. The normalized first, second, and third order structure functions for various ebb and flood intervals demonstrate distinct exponents and plateau values, implying different fractal characteristics between the ebb and flood flows, as shown in Figure 3. All sections show structure function slope discrepancy between the ebb and the flood flow. Here, the second order structure functions S_2 of the first and third sections are selected to highlight this

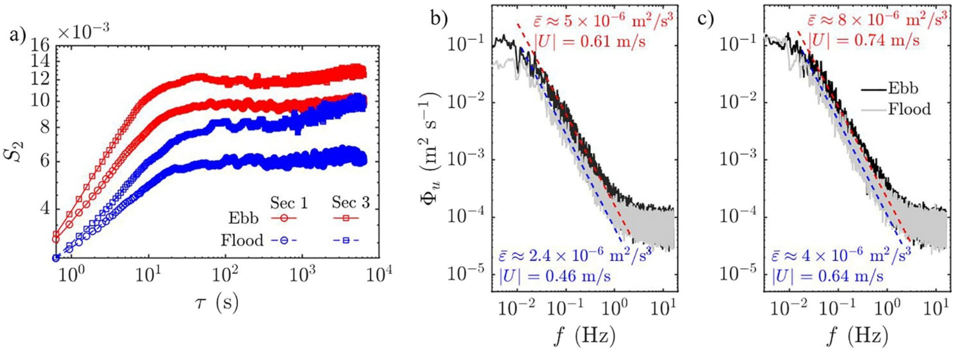

Figure 4. Comparison of ebb and flood flows in the first and third sections (Figure 1). (a) second-order structure function, S_2, (b) Streamwise velocity spectrum Φ_u for the first section, and (c) Φ_u for the third section.

discrepancy between the ebb and flood flow in Figure 4 along with the streamwise velocity spectrum of the ebb and flood flow sections to compare with the theoretical S_2 scaling within the inertial subrange of isotropic turbulence proposed by Kolmogorov (1941):

$$S_2(r) \sim (\bar{\varepsilon} r)^{2/3} = C_1 (\bar{\varepsilon} r)^{2/3}. \tag{11}$$

Here, C_1 is the Kolmogorov constant. The S_2 distributions reveal a "slope" difference within the inertial subrange that is not captured in the velocity spectrum, highlighting the limitation of a linear model of spectral analysis. The linear spectral analysis assumes that the irregularity in data has the same form at the beginning, middle, and end of the time series Kelty-Stephen et al. (2023), that is, there is no long-range dependence in the data.

Two types of normalization are employed on S_2, as shown in Figures 5a and 5b, as an attempt to collapse the S_2 magnitude between different sections of the ebb and flood flows. The first normalization follows the Taylor's frozen field hypothesis, which allows a linear transformation between spatial separation r and time lag τ, such that $r \equiv \bar{u}\tau$, transforming Equation 11 to $S_2(\tau) = C_1(\overline{u\varepsilon} r)^{2/3}$. The second normalization follows the random

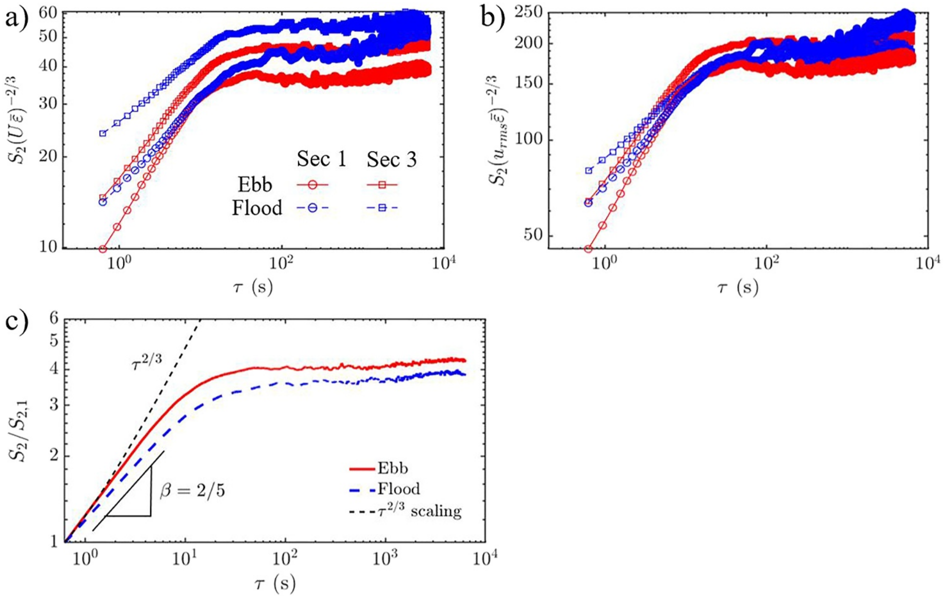

Figure 5. Normalized second-order structure function for Section 1 (circular symbols) and Section 3 (square symbols) of ebb (red) and flood (blue) flows (Figure 1) with (a) normalization by $U\bar{\varepsilon}^{2/3}$ following the Taylor frozen field hypothesis and (b) normalization by $u_{\text{rms}}\bar{\varepsilon}^{2/3}$ following the random sweeping field hypothesis. (c) Averaged second-order structure function across all sections for ebb and flood flows.

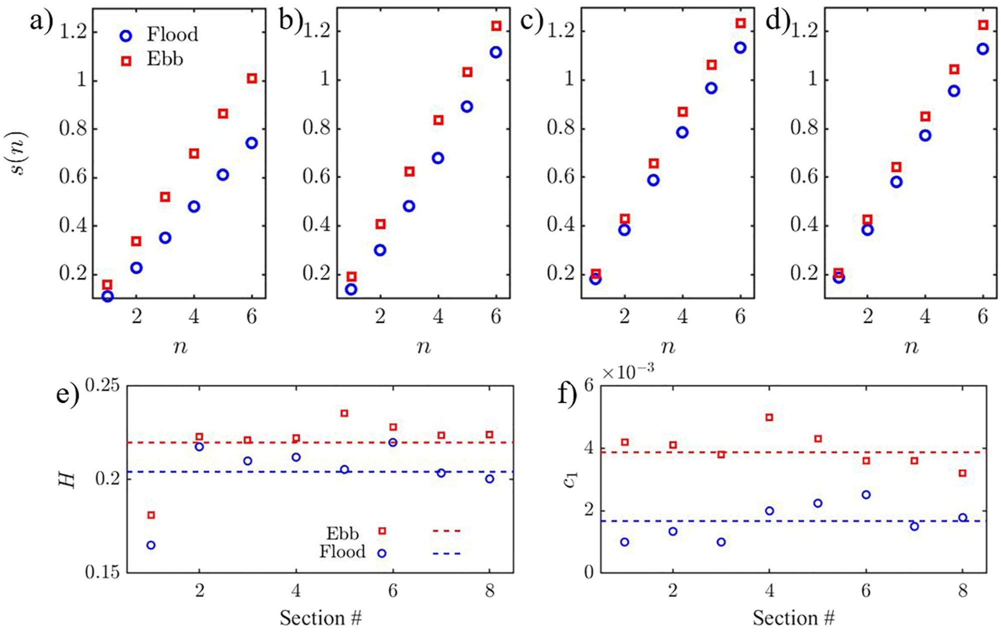

Figure 6. Scaling (slope) of n-th order structure functions for the ebb and flood flows of selected tidal sections (Figure 1): (a) Section 1, (b) Section 3, (c) Section 5, and (d) Section 7. (e) Hurst exponent H and (f) intermittency exponent c_1 estimated from structure functions for ebb and flood flow sections, with dashed lines indicating the averaged values across all sections.

sweeping hypothesis and gives $S_2(\tau) = C_1(\bar{\varepsilon} u_{\mathrm{rms}} r)^{2/3}$. Our data show that the second normalization provides a better collapse between the ebb and flood flow sections. This is due to the assumption of Taylor's frozen field hypothesis that $u_{\mathrm{rms}}/\bar{u} \ll 1$ failing on the detrended velocity fluctuation time series; thus, the eddies advected past the measurement probe may evolve over the measurement duration.

Despite the normalization based on the random field hypothesis better collapsing the magnitude of S_2 between various flow sections, there are slope deviations within the inertial subrange for different sections of the flow. Figure 5c shows the ensemble-averaged S_2 of all eight ebb and flood flow sections defined in Figure 1. The slope discrepancy between ebb and flood sections demonstrates a deviation from the theoretical 2/3 scaling as indicated in Equation 11. This deviation is indicative of intermittency and multifractality within the flow. The degree of intermittency and fractality can be estimated using a scaling exponent s defined by $S_n(\tau) \sim \tau^{s(n)}$. This power-law distribution is observed for $0.0625 \leq \tau \leq 10$ s for structure functions up to an order of $n = 6$. The scaling exponent s versus order n for selected sections is provided in Figures 6a–6d. The Hurst exponent H and the intermittency parameter c_1 are related to the linear and quadratic coefficients of the fit of the structure function scaling exponent $s(n)$ to order n (Davis et al., 1994; Frisch, 1995), such that $s(n) = Hn - c_1 n^2$.

The estimated Hurst component, H, and intermittency coefficient, c_1, are depicted in Figures 6e and 6f for all sections (Figure 1) with the ensemble-averaged values indicated by dashed lines. Larger values of H and c_1 are observed for the ebb sections, suggesting stronger long-range dependence and intermittency in the ebb flow sections. Despite these insights, it is important to note that the Hurst component computed by $s(n)$ does not account for multifractal behavior. Detailed multifractal analysis and higher-order spectral moments are conducted to further explore the long-range dependence and intermittent characteristics within the flow.

4.2. Multifractal Analysis

Detrending moving average (DMA) analysis is conducted to further explore the scaling behavior of the first ebb and flood segment at the nodule point tidal site (Figures 7a and 7b). The log-log representation of σ_{DMA} versus window size n reveals distinct slope scalings for different timescales, demonstrating the multifractal characteristic of the time series. This indicates that the Hurst exponent estimated by structure functions is insufficient to fully describe the multifractal characteristics of the time series in tidal flow sections requiring multifractal analysis.

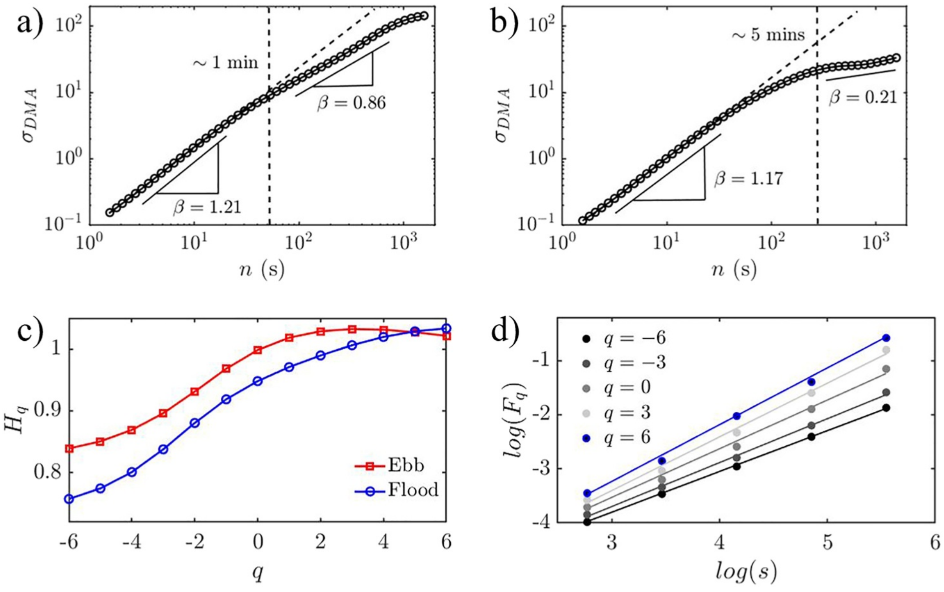

Figure 7. Evaluation of the Hurst exponent through the scaling of σ_{DMA} vs. window size n for Section 1: (a) ebb flow and (b) flood flow. (c) q-th order Hurst component H_q for the first flood and ebb segment, and (d) q-th order RMS along with their corresponding regression line calculated using MF-DFA.

A distinct change at the timescale of approximately one and 5 min is observed for the ebb and the flood flow section in Figures 7a and 7b. A slight change in scaling slope is also noted for the ebb flood at a shorter timescale (approximately 1 min), though this change is much less pronounced compared to that of the flood flow. This highlights a difference in periodicity between ebb and flood flows. The log-log representation of $\sigma_{DMA}(n)$ versus n are characterized by two scaling regions. Each of them is fitted to determine a Hurst exponent. Specifically, at the indicated timescales, the slope (power) values for ebb and flood flow sections are nearly identical on a small scale (only Section 1 is shown here for brevity), with values of 1.21 ± 0.02 for ebb flows and 1.17 ± 0.01 for flood flows, suggesting similar periodicity properties. However, the Hurst exponent values at the larger timescale are 0.86 ± 0.03 and 0.23 ± 0.05 for the ebb and flood flow sections. The ebb section, with $H > 0.5$, demonstrates a persistent characteristic, whereas the flood section, with $H < 0.5$, exhibits a significant magnitude change indicative of antipersistent behavior.

Here, we use MF-DFA to explore the multifractal characteristics of ebb and flood flow sections. The log-log relationship between the q-th order root mean square fluctuation F_q and scale s is depicted in Figures 7c and 7d. The scaling behavior for segments exhibiting large fluctuations is captured by the general Hurst exponent for positive q values, whereas negative q values characterize segments with comparatively small fluctuations. Furthermore, the singularity spectrum $D(q)$ can be derived from the generalized Hurst exponent $H(q)$.

The $F_q(s)$ curves vs. s are fitted using least squares regression for each value of q, resulting in the generalized q-th order Hurst component H_q as illustrated in Figure 7c. The varying H_q values highlight the distinct multifractal behaviors of the flood and ebb flows. Specifically, larger H_q values are observed for $q \leq 5$ in the flood segment. A smaller difference between flood and ebb flows is noted for higher positive q values, attributable to the plateau observed in the flood segment for $q > 1$. Nevertheless, a lower slope in the H_q vs. q plot is evident for positive q values in both segments. This suggests that the q-th order RMS is relatively less sensitive to local fluctuations of large magnitudes in both segments with this effect being more pronounced in the ebbed segments. It is worth noting that a positive slope is observed in Figure 7c attributed to the significant differences between F_q values at larger s scales. This result is surprising because the opposite trend is more commonly observed. Namely, larger segments spanning several local periods, characterized by minor and major fluctuations, are anticipated to average their magnitude differences.

The q-th order Hurst exponent, H_q, can be transformed into the multifractal spectrum D_q. The temporal variation of the local Hurst exponent is presented as a probability distribution in Figure 8a, and the multifractal spectrum D_q

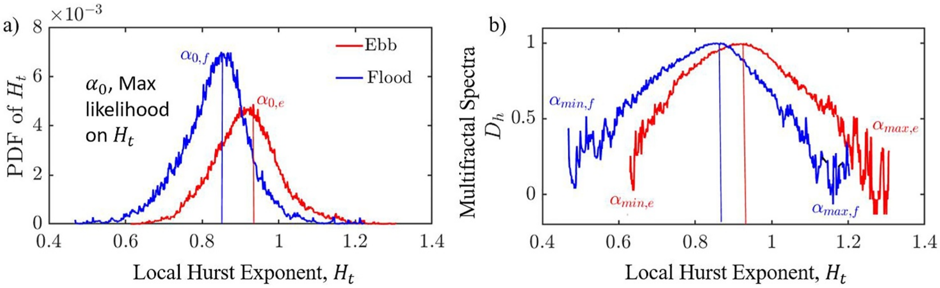

Figure 8. (a) Probability density function (PDF) distribution of local Hurst exponent H_t and (b) the multifractal spectrum D_h for the first flood and ebb segment.

is shown as the normalized probability distribution in log-coordinates in Figure 8b. The multifractal spectrum D_h versus H_t is characterized by α_0, the maximum likelihood of the local Hurst exponent; the width/range of the D_h spectrum, defined as $\alpha_{\max} - \alpha_{\min}$; and the skewness A of the D_h spectrum, defined by:

$$A = \frac{\alpha_{\max} - \alpha_0}{\alpha_0 - \alpha_{\min}}. \tag{12}$$

A value of $A > 1$ indicates a right-skewed spectrum, whereas $A < 1$ indicates a left-skewed spectrum. The computed values of α_0, range, and A for selected ebb and flood flow segments are presented in Figure 9.

We observe that at the nodule point, WA tidal site a larger α_0 for the ebb flows corresponds well with the H values obtained through the structure function method. Despite the higher Hurst component for the ebb flow, we note a narrower D_h width. By definition, the width of the multifractal spectrum indicates the range of temporal variation in the local scale-invariant structure; hence, a narrower width suggests a lower degree of multifractality for the ebb flow segments. The ebb flow segments exhibit an A value greater than unity, whereas for flood flows, $A < 1$. This implies that ebb flow segments at nodule point are less affected by local fluctuations of large magnitudes, whereas flood flows show insensitivity to fluctuations of smaller magnitudes. These results align with those depicted in Figure 7c, demonstrating that H_q for the ebb flow tends to plateau for $n \geq 2$.

4.3. On the Multifractality in Tidal Flows

Two main sources of multifractality have been identified (Kantelhardt et al., 2002; Movahed et al., 2006): first, the presence of varying long-range correlations within the time series for small- and large-scale fluctuations, where the autocorrelation exhibits a decay rate slower than that of exponential decay, and second, the existence of nonlinear correlations and intermittent events within the time series, leading to a heavy-tailed probability distribution function.

Two sets of surrogate data are generated to verify the source of multifractality. The first set of data is produced by randomly permuting the temporal order of the raw velocity time series, effectively breaking all temporal correlations. The second type of surrogate data is generated using the iterative amplitude-adjusted Fourier transform (IAAFT) algorithm (Schreiber & Schmitz, 1996). This algorithm aims to construct a time series that mimics the

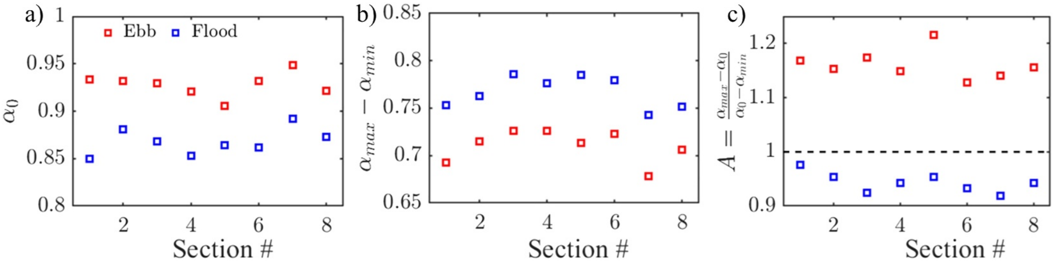

Figure 9. Characterization of the multifractal spectrum for all Nodule Point, WA sections: (a) α_0, (b) $\alpha_{\max} - \alpha_{\min}$, and (c) $A-$ quantifying the symmetry of the spectrum.

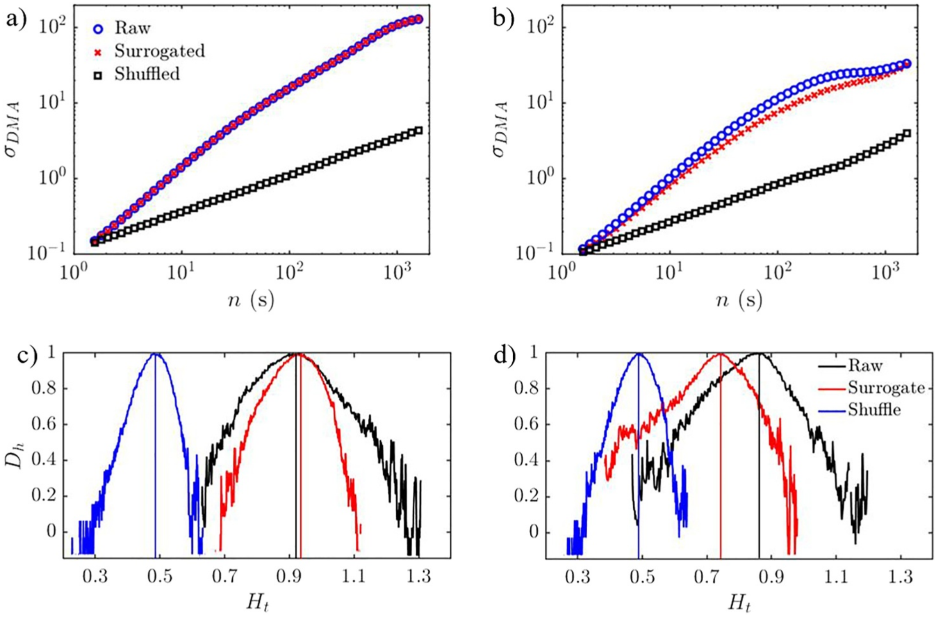

Figure 10. Evaluation of σ_{DMA} scaling versus window size n for the raw (black), permuted (blue), and surrogate (red) time series of (a) the first ebb, and (b) the first flood segment (Figure 1). Multifractal spectrum of the original (black), permuted (blue), and surrogate (red) time series for (c) the first flood segment, and (d) the first ebb segment.

best-fitting linear model of the original series, thereby testing the null hypothesis that multifractality reflects nonlinear interactions between timescales. The IAAFT algorithm consists of four steps: First, a time series with a Gaussian distribution is generated, matching the original signal in length, mean, and variance. This is done by storing the amplitude spectrum of the original series' Fourier transform by their rank order. Second, the series is randomized to eliminate possible nonlinear dynamics. Third, the amplitude spectrum in the randomized series is replaced with that of the original series using inverse Fourier transformation. Finally, the rank-ordered values of the inverse Fourier series are matched to the rank-ordered values in the original series. This procedure is repeated for 25 iterations to mitigate the risk of distorting the amplitude spectrum during the rank-matching step. The IAAFT algorithm enables the generation of a surrogate time series that maintains the original series' linear temporal correlations.

The application of the detrending moving average (DMA) analysis to both permuted and surrogate time series is presented in Figures 10a and 10b. Distinct scaling characteristics for the ebb and flood flow segments suggest that different segments likely contribute differently to the source of multifractality. Specifically, the first ebb flow section, as shown in Figure 10a, reveals an overlapping scaling between the raw and surrogate data. An almost linear scaling is observed for the permuted ebb time series. Conversely, two scaling ranges are still evident for the permuted flood flow, whereas it displays a nonoverlapping scaling between the raw and surrogate time series.

The multifractal spectra, D_h, provided in Figures 10c and 10d, show $\alpha_0 \approx 0.5$ for permuted ebb and flood flow data. The characterization of multifractal spectra is depicted in Figure 11. As expected, the permuted data exhibits an α_0 slightly lower than 0.5, indicating that the long-range temporal dependence is almost absent. The D_h spectrum width of permuted data is significantly reduced, demonstrating that long-range dependence is the primary source of multifractality. However, it is crucial to note that nonlinearity and intermittent events also contribute to multifractality, as the permuted data still show considerable spectrum width and do not become monofractal. Note that the permuted and surrogate data demonstrated a left-skewed spectrum with a much smaller $A < 1$ compared to the raw data A values. This suggests that the long-range dependence on nonlinear events may be most susceptible to large-scale fluctuations; thus, indicating that nonlinear interaction across timescales is the source of multifractal behavior at large scales (i.e., $q > 0$ in Figures 7c and 7d).

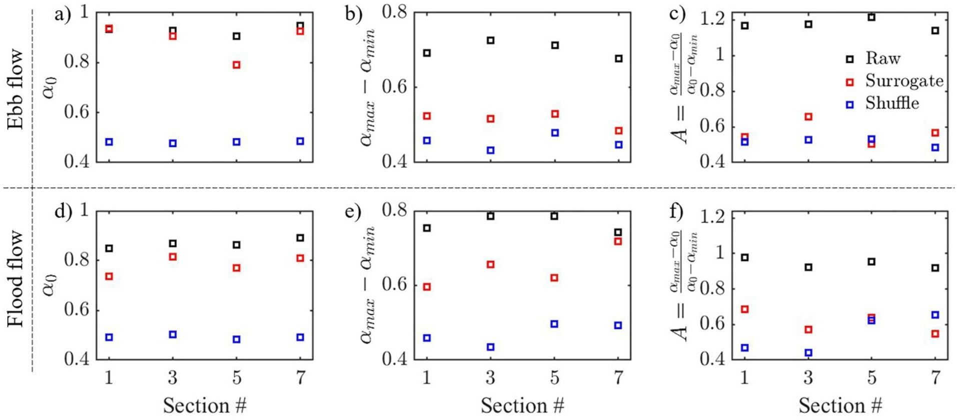

Figure 11. Characterization of the multifractal spectrum of (a, b, c) ebb flow sections, and (d, e, f) flood flow sections. (a, d) α_0, (b, e) $\alpha_{\max} - \alpha_{\min}$, and (c, f) A quantifying symmetry of the spectrum.

4.4. Intermittent Events

Further evaluation of intermittency is conducted by examining the velocity fluctuation time series u' and the first- and second-order velocity increments, $\Delta u'$ and $\Delta^2 u'$, as depicted in Figure 12. These increments do not seem to exhibit more intermittent events than the raw velocity fluctuation time series for ebb and flood flows. This observation is aligned with the probability density functions of the three quantities, normalized by their respective standard deviations, shown in Figure 13a. Here, a longer tail is observed for the raw velocity fluctuation, whereas the velocity increments generally follow a Gaussian distribution. The classical measure of intermittency, flatness $F4$, is calculated for all sections to quantify the deviation from the Gaussian distribution. Flatness $F4$ is defined as the normalized fourth-order moment of the PDF, $F4 = \mu_4/\mu_2^2$, where μ_n represents the n-th order moment of the PDF.

The summary of flatness is shown in Figures 13b and 13c for the ebb and flood flow sections. The probability density function departs from a Gaussian distribution for u', whereas the velocity increments display a slight deviation from a Gaussian distribution with a flatness value approaching 3. This finding is quite unexpected, indicating that the tidal site exhibits more intermittency at larger scales, in contrast to the trend observed in canonical turbulence studies (Batchelor & Townsend, 1949; Lortie & Mydlarski, 2022), which noted an increase in flatness factors with higher orders of differentiation. Also, Figures 13b and 13c reveals that the ebb flow sections have a higher flatness compared to the flood sections aligning with estimations obtained using the structure function method depicted in Figure 6f.

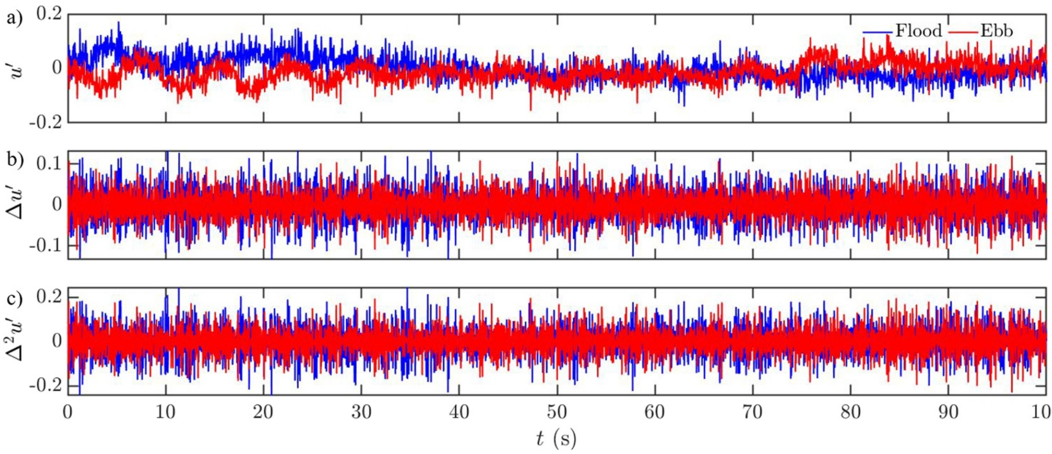

Figure 12. Sample time series of (a) detrended streamwise velocity fluctuations u', (b) first-order velocity increment $\Delta u'$, and (c) second-order velocity increment $\Delta^2 u'$.

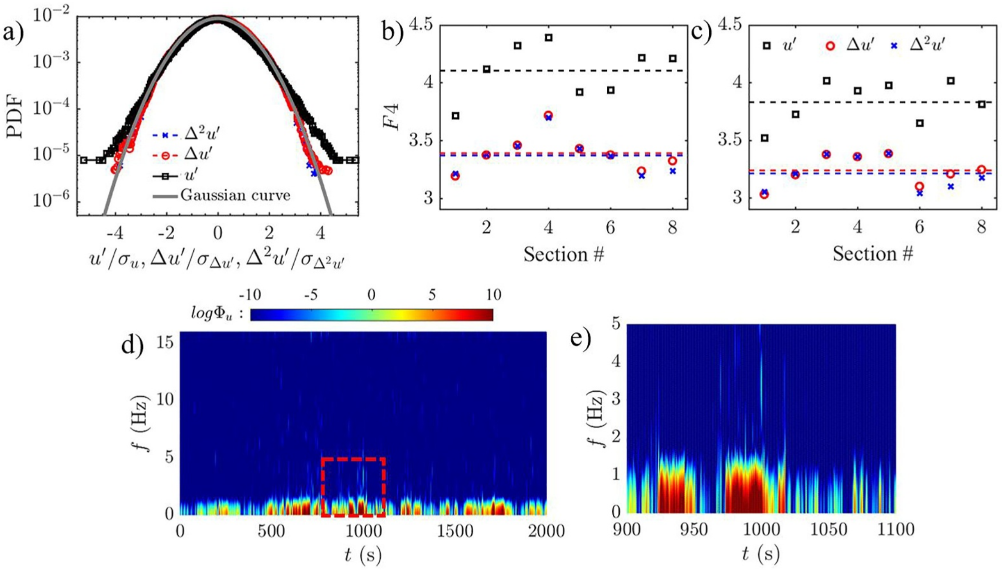

Figure 13. (a) Probability density functions for u', $\Delta u'$, and $\Delta^2 u'$. (b, c) Flatness of the PDF distribution for all sections: (b) for ebb flows and (c) for flood flows with a dashed line representing the averaged value across all sections. (d) Spectrogram generated from the short-time Fourier transform, and (e) a focused view of the area within the red dashed box from (d), showing strong activity for $f \leq 5$ Hz.

Although flatness is commonly used to indicate the level of intermittency, it does not offer a detailed account of how intermittent events are distributed across scales. To explore the scale dependency of intermittency events, higher-spectral moments are computed using a short-time Fourier transform (STFT), as discussed in Section 3.1. Here, the time series of the velocity fluctuations is first detrended (Cheng et al., 2024) before the STFT algorithm is applied; an example of the detrended data series is shown in Figure 2g. For brevity, only the results for spectral kurtosis are shown, as the spectral skewness exhibited a similar trend. Figures 13d and 13e display the spectrogram obtained from STFT using a relatively large Hamming window of $N = 1024$ samples. The spectrogram reveals low-frequency spikes indicative of the presence of intermittent events, whereas the high-frequency region shows minimal energy consistent with the PDF distribution observed in Figure 13a. A detailed view of the low-frequency segment for selected times $900 \geq t \leq 1100$ s is shown in Figure 13e, illustrating that the duration of strong intermittent events ranges approximately from 5 to 20 s, that is, 160 to 640 samples. It serves as a guide for optimizing the filtering window size in the computation of high-order spectral moments.

The impact of different filtering window sizes on the spectral Kurtosis, $\tilde{K}$, for the initial ebb and flood sections is illustrated in Figure 14 using Hamming windows of 128, 256, and 512 samples. An additional 0.95 confidence level interval is depicted using black dashed lines. Although a shorter window may enhance the higher-order spectral moments, this comes at the cost of reduced frequency resolution, as shown in Figure 14a. This is because the minimum frequency that can be resolved is determined by the length of the filtering window, as discussed in Section 3.1, which may not be suitable for this analysis. Conversely, longer windows encompass a broader range of frequencies. Figure 14c shows that a filtering window size of 512 samples successfully captures low-frequency deviations from Gaussianity and provides sufficient frequency resolution to distinguish between two distinct peaks for $f \leq 1$ Hz. This finding, as confirmed in Figure 14, indicates that a filtering window size aligned with the duration of transient events yields optimized results for spectral Kurtosis, $\tilde{K}$ (Lortie, 2021). Therefore, a Hamming window with a length of 512 samples is selected for subsequent analysis.

Spectral kurtosis $\tilde{K}$ of the selected section of ebb and flood flows from nodule, WA, are provided in Figures 15a–15d shown with their respective streamwise velocity spectrum. A nonmonotonically increasing $\tilde{K}$ is observed within the inertial subrange for the tidal flows; a similar trend is also observed at the East River, NY Tidal Energy site, not shown here for brevity. Instead, $\tilde{K}$ reaches the peak value and fluctuates between the beginning to the middle of the inertial subrange, that is, $\sim 0.1 - 0.5$ Hz for tidal flow at nodule point site and starts decreasing for even higher frequency. Figure 15 illustrates the ability of spectral kurtosis to detect and isolate each scale's

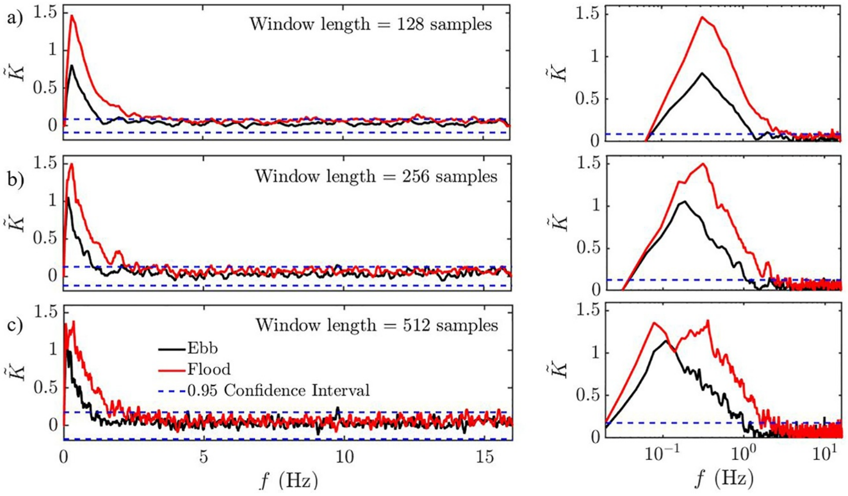

Figure 14. Impact of filtering window lengths on Section 1 ebb and flood flow (Figure 1), with a 95% confidence interval (dashed line). Hamming window sizes: (a) 128, (b) 256, (c) 512 samples; frequencies are shown in linear scale (left) and log scale (right) to highlight low-frequency events.

contribution to non-Gaussianilty within the time series, which allows us to evaluate the relative intermittency level at each scale. The magnitude of $\tilde{K}$ reveals that the ebb flow sections demonstrate stronger intermittency across all scales compared to flood flow sections aside from the higher overall intermittency level reported using structure function and PDF analysis (Figures 6f and 13b, 13c); also, the difference in $\tilde{K}$ magnitudes reduce beyond $f \gtrsim 0.5$ Hz. Similar $\tilde{K}$ trend is observed for the velocity time series obtained from East River, NY tidal energy site in Figure 15e, validating that the intermittency characteristics of tidal flows differ from the monotonically increasing $\tilde{K}$ in grid turbulence and wall-bounded turbulent flows (Lortie, 2021; Lortie & Mydlarski, 2022).

5. Discussions

The analysis of tidal flows at the NP site provides crucial insights into their multifractal and intermittent characteristics, revealing distinct directional dependencies and varying degrees of long-range dependence and sensitivity to large fluctuations. These factors can modulate various environmental and hydrological phenomena.

Multifractal detrended fluctuation analysis (MF-DFA) and spectral kurtosis were instrumental in uncovering the multifractal and intermittent features. MF-DFA revealed the scale-invariant nature of multifractality, whereas

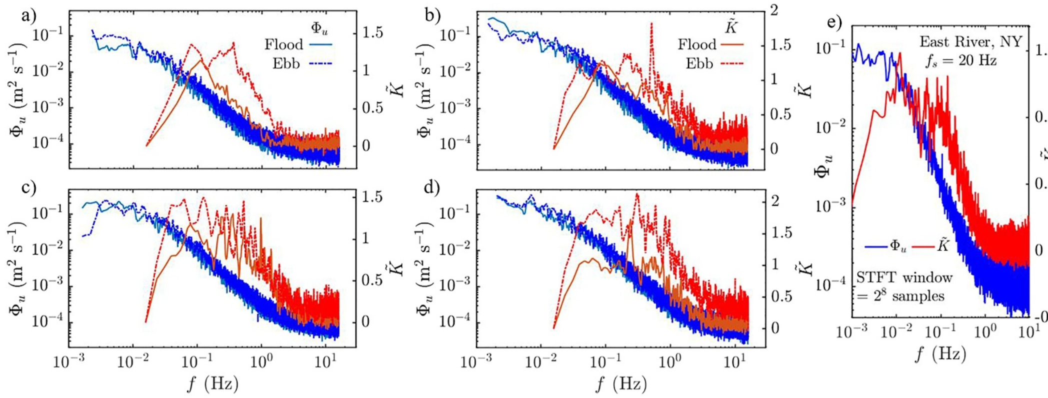

Figure 15. Comparison between ebb (solid lines) and flood (dashed lines) flows of streamwise velocity spectrum Φ_u and spectral kurtosis $\tilde{K}$ for selected sections: (a) Section 1, (b) Section 3, (c) Section 5, (d) Section 7 from nodule point, WA, and (e) Φ_u and $\tilde{K}$ for East River, NY tidal site.

spectral kurtosis showcased the nonmonotonic behavior of intermittency across different frequency scales, a phenomenon not typically observed in turbulence studies. The multifractal spectrum D_h indicated higher LRD for the ebb sections, whereas the wider left-skewed D_h spectrum for flood sections suggested higher multifractality and susceptibility to large-scale fluctuations.

Two sets of surrogate time series were used to explore the origin of multifractality. The width of the D_h spectrum significantly reduced for the temporally permuted ebb and flood sections, with $H \approx 0.5$, indicating a slow decay in autocorrelation in the original time series due to temporal LRD is the primary source of multifractality. However, the IAAFT algorithm generated phase-permuted data also exhibited a narrower D_h spectrum width, suggesting a non-negligible contribution to multifractality aside from the contribution of LRD. Both temporal- and phase-permuted surrogate time series for ebb and flood flows showed a pronounced left-skewed D_h spectrum, indicating that the long-range dependence of nonlinear intermittent events plays a crucial role in the large-scale multifractal characteristics.

The fourth-order spectral moments, spectral kurtosis $\tilde{K}$ indicated higher intermittency levels across all frequency scales in ebb flow sections and unveiled a unique tidal flow intermittency pattern, diverging from the patterns observed in wall-bounded and grid turbulence. The spectral kurtosis pattern demonstrated a plateau at the beginning of the inertial subrange, and decay in $\tilde{K}$ began as the frequency approached the middle of the inertial subrange, indicating a Gaussian-like PDF distribution for small-scale events at both investigated tidal sites.

It is worth highlighting the effectiveness of using multifractal detrended fluctuation analysis (MF-DFA) and spectral kurtosis to reveal multifractal and intermittent attributes of tidal flows. The flood and ebb flow multifractal characteristics at nodule point, WA, may differ due to a combination of physical and environmental factors, including bathymetric complexity, channel geometry, and wind forcing mechanisms. At nodule point, WA, the tidal dynamics are likely influenced by local bathymetric features, such as channel constrictions (Moegling & Cochrane, 2022) that may amplify the flood dominance and leads to a wider multifractal spectrum and demonstrates lower overall turbulence intermittency compared to ebb flows (Friedrichs & Aubrey, 1988). Also, difference in turbulence scaling and intermittency can be resulted from stratification and vertical mixing during flood and ebb tides (Burchard & Baumert, 1998) and reflected in multifractal flow properties.

Finally, this study serves as an initial step toward integrating fractal and intermittent characteristics of tidal/wind behavior into turbulence spectrum modeling, aiding in the design, operation, and maintenance of tidal/wind turbines and offering valuable insights for estimating the LCOE. Also, the directional variations in multifractality and intermittency impact tidal energy extraction and environmental management, informing sustainable coastal development and ecosystem conservation strategies, as tidal flows significantly shape coastal landscapes and influence marine habitats.

6. Conclusions

This study provides a comprehensive analysis of tidal flows' multifractal and intermittent characteristics, offering insights into their complex dynamics. Using detrending moving average (DMA) and multifractal detrended fluctuation analysis (MF-DFA), we uncovered particular differences between ebb and flood flow sections at the nodule point, WA, and East River, NY, tidal sites. Our findings revealed that ebb flows exhibit higher Hurst exponents and overall intermittency compared to flood flows at the investigated tidal sites, suggesting distinct flow dynamics and energy distribution mechanisms between the two phases of the tidal cycle.

Through detailed methodologies such as DMA and MF-DFA, we uncovered the presence of multiple fractal scalings within the tidal flow data, highlighting the intricate multifractal nature of these flows. This multifractal behavior indicates a hierarchical organization of turbulent structures across different scales with implications for energy dissipation and transfer processes within the flow. Also, inspecting scale-dependent intermittency levels using spectral kurtosis provided further insights into the statistical properties of turbulent fluctuations, revealing a Gaussian-like PDF distribution for small-scale events.

By highlighting the importance of integrating multifractal analysis into spectral models, this work advances our understanding of turbulent systems and offers valuable tools for optimizing energy capture in renewable energy devices such as tidal turbines at the specific tidal site. Note that external factors such as wind forcing and freshwater input may also induce spatial and temporal variations in the flow structure, thus impacting the multifractal characteristics (Lai et al., 2018; Wei et al., 2021). Future work will investigate the long-range dependence and intermittency patterns across multiple tidal sites, incorporating data at various heights and geographic patterns to establish links between multifractal behavior and underlying physical characteristics. Furthermore, our findings show the need for continued research to refine numerical models and accurately predict environmental flows particularly in sustainable coastal development and renewable energy generation, where turbulent dynamics play a crucial role.

Data Availability Statement

Data sets are available over DOE's Open EI, MHK data repository, https://mhkdr.openei.org/ and code are available from Cheng et al. (2024).

Acknowledgments
Sandia National Laboratories is a multimission laboratory managed and operated by National Technology and Engineering Solutions of Sandia, LLC., a wholly owned subsidiary of Honeywell International, Inc., for the U.S. Department of Energy's National Nuclear Security Administration under contract DE-NA0003525. This paper describes objective technical results and analysis. Any subjective views or opinions that might be expressed in the paper do not necessarily represent the views of the U.S. Department of Energy or the United States Government.

References

Adarsh, S., Dharan, D. S., Nandhu, A., Anand Vishnu, B., Mohan, V. K., & Wątorek, M. (2020). Multifractal description of streamflow and suspended sediment concentration data from Indian river basins. *Acta Geophysica*, *68*(2), 519–535. https://doi.org/10.1007/s11600-020-00407-2

Ali, N., & Cal, R. B. (2019). Scale evolution, intermittency and fluctuation relations in the near-wake of a wind turbine array. *Chaos, Solitons & Fractals*, *119*, 215–229. https://doi.org/10.1016/j.chaos.2018.12.018

Antoni, J., & Randall, R. B. (2006). The spectral kurtosis: Application to the vibratory surveillance and diagnostics of rotating machines. *Mechanical Systems and Signal Processing*, *20*(2), 308–331. https://doi.org/10.1016/j.ymssp.2004.09.002

Anup, K., Whale, J., & Peinke, J. (2021). An investigation of the impact of turbulence intermittency on the rotor loads of a small wind turbine. *Renewable Energy*, *169*, 582–597. https://doi.org/10.1016/j.renene.2021.01.049

Bashirzadeh Tabrizi, A., Wu, B., Whale, J., & Shahabi Lotfabadi, M. (2019). Using Turbsim stochastic simulator to improve accuracy of computational modelling of wind in the built environment. *Wind Engineering*, *43*(2), 147–161. https://doi.org/10.1177/0309524x18780388

Batchelor, G. K., & Townsend, A. A. (1949). The nature of turbulent motion at large wave-numbers. *Proceedings of the Royal Society of London. Series A. Mathematical and Physical Sciences*, *199*(1057), 238–255.

Bossuyt, J., Howland, M., Meneveau, C., & Meyers, J. (2016). Measuring power output intermittency and unsteady loading in a micro wind farm model. In *34th wind energy symposium. 1992*.

Brown, J., & Davies, A. (2010). Flood/ebb tidal asymmetry in a shallow sandy estuary and the impact on net sand transport. *Geomorphology*, *114*(3), 431–439. https://doi.org/10.1016/j.geomorph.2009.08.006

Burchard, H., & Baumert, H. (1998). The formation of estuarine turbidity maxima due to density effects in the salt wedge. a hydrodynamic process study. *Journal of Physical Oceanography*, *28*(2), 309–321. https://doi.org/10.1175/1520-0485(1998)028<0309:tfoetm>2.0.co;2

Byon, E. (2013). Wind turbine operations and maintenance: A tractable approximation of dynamic decision making. *IIE Transactions*, *45*(11), 1188–1201. https://doi.org/10.1080/0740817x.2012.726819

Cheng, S., Neary, V. S., & Chamorro, L. P. (2024). On detrending stream velocity time series for robust tidal flow turbulence characterization. *Ocean Engineering*, *300*, 117427. https://doi.org/10.1016/j.oceaneng.2024.117427

Chowdhury, M., Rahman, K., Selvanathan, V., Nuthammachot, N., Suklueng, M., Mostafaeipour, A., et al. (2021). Current trends and prospects of tidal energy technology. *Environment, Development and Sustainability*, *23*(6), 8179–8194. https://doi.org/10.1007/s10668-020-01013-4

Davis, A., Marshak, A., Wiscombe, W., & Cahalan, R. (1994). Multifractal characterizations of nonstationarity and intermittency in geophysical fields: Observed, retrieved, or simulated. *Journal of Geophysical Research*, *99*(D4), 8055–8072.

Dias, N. L., Crivellaro, B. L., & Chamecki, M. (2018). The Hurst phenomenon in error estimates related to atmospheric turbulence. *Boundary-Layer Meteorology*, *168*(3), 387–416. https://doi.org/10.1007/s10546-018-0353-7

Dike, C. C., & Agunwamba, J. C. (2012). A study on the effects of tide on sedimentation in estuaries of the Niger delta, Nigeria. *Journal of Urban and Environmental Engineering*, *6*(2), 86–93. https://doi.org/10.4090/juee.2012.v6n2.086093

Dronkers, J. (1986). Tidal asymmetry and estuarine morphology. *Netherlands Journal of Sea Research*, *20*(2–3), 117–131. https://doi.org/10.1016/0077-7579(86)90036-0

Dwyer, R. F. (1983). A technique for improving detection and estimation of signals contaminated by under ice noise. *Journal of the Acoustical Society of America*, *74*(1), 124–130. https://doi.org/10.1121/1.389729

Egbert, G. D., & Ray, R. D. (2003). Semi-diurnal and diurnal tidal dissipation from Topex/Poseidon altimetry. *Geophysical Research Letters*, *30*(17). https://doi.org/10.1029/2003gl017676

EIA. (2023). *Projected electricity generation worldwide in 2022 with a forecast to 2050, by energy source (in 1,000 terawatt-hours)*. Statista inc. Retrieved from https://www.statista.com/statistics/238610/projected-world-electricity-generation-by-energy-source/. Accessed: March 26, 2024.

El-Thalji, I., & Liyanage, J. P. (2012). On the operation and maintenance practices of wind power asset: A status review and observations. *Journal of Quality in Maintenance Engineering*, *18*(3), 232–266. https://doi.org/10.1108/13552511211265785

Foley, J. T., & Gutowski, T. G. (2008). Turbsim: Reliability-based wind turbine simulator. In *2008 IEEE international symposium on electronics and the environment* (pp. 1–5).

Fong, D. A., Monismith, S. G., Stacey, M. T., & Burau, J. R. (2009). Turbulent stresses and secondary currents in a tidal-forced channel with significant curvature and asymmetric bed forms. *Journal of Hydraulic Engineering*, *135*(3), 198–208. https://doi.org/10.1061/(asce)0733-9429(2009)135:3(198)

Friedrichs, C. T., & Aubrey, D. G. (1988). Non-linear tidal distortion in shallow well-mixed estuaries: A synthesis. Estuarine. *Coastal and Shelf Science*, *27*(5), 521–545. https://doi.org/10.1016/0272-7714(88)90082-0

Frisch, U. (1995). *Turbulence: The legacy of an Kolmogorov*. Cambridge University Press.

Geng, L., Gong, Z., Zhou, Z., Lanzoni, S., & D'Alpaos, A. (2020). Assessing the relative contributions of the flood tide and the ebb tide to tidal channel network dynamics. *Earth Surface Processes and Landforms*, *45*(1), 237–250. https://doi.org/10.1002/esp.4727

Gunawan, B., Neary, V., & Colby, J. (2014). Tidal energy site resource assessment in the East River tidal strait, near Roosevelt Island, New York. *Renewable Energy*, *71*, 509–517. https://doi.org/10.1016/j.renene.2014.06.002

Hammons, T. J. (1993). Tidal power. *Proceedings of the IEEE*, *81*(3), 419–433. https://doi.org/10.1109/5.241486

Hu, Y., Bao, W., Tu, X., Li, F., & Li, K. (2019). An adaptive spectral kurtosis method and its application to fault detection of rolling element bearings. *IEEE Transactions on Instrumentation and Measurement*, *69*(3), 739–750. https://doi.org/10.1109/tim.2019.2905022

Huckerby, J., Jeffrey, H., de Andres, A., & Finlay, L. (2016). An international vision for ocean energy, 2016. www.ocean-energy-systems.org

Hurst, H. E. (1951). Long-term storage capacity of reservoirs. *Transactions of the American Society of Civil Engineers*, *116*(1), 770–799. https://doi.org/10.1061/taceat.0006518

Jay, D. A., & Musiak, J. D. (1994). Particle trapping in estuarine tidal flows. *Journal of Geophysical Research*, *99*(C10), 20445–20461. https://doi.org/10.1029/94jc00971

Jonkman, B. J. (2009). *Turbsim user's guide: Version 1.50* (Tech. Rep.). National Renewable Energy Lab.(NREL).

Kantelhardt, J. W., Zschiegner, S. A., Koscielny-Bunde, E., Havlin, S., Bunde, A., & Stanley, H. E. (2002). Multifractal detrended fluctuation analysis of nonstationary time series. *Physica A: Statistical Mechanics and its Applications*, *316*(1–4), 87–114. https://doi.org/10.1016/s0378-4371(02)01383-3

Kelley, N., & Jonkman, B. (2005). *Overview of the TurbSim stochastic inflow turbulence simulator* (Tech. Rep.). National Renewable Energy Lab. (NREL).

Kelty-Stephen, D. G., Lane, E., Bloomfield, L., & Mangalam, M. (2023). Multifractal test for nonlinearity of interactions across scales in time series. *Behavior Research Methods*, *55*(5), 2249–2282. https://doi.org/10.3758/s13428-022-01866-9

Kempener, R., & Neumann, F. (2014). *Tidal energy technology brief* (pp. 1–34). International Renewable Energy Agency (IRENA).

Kolmogorov, A. N. (1941). The local structure of turbulence in incompressible viscous fluid for very large Reynolds. Numbers. *Doklady Akademii Nauk SSSR*, *30*, 301.

Lai, W., Pan, J., & Devlin, A. T. (2018). Impact of tides and winds on estuarine circulation in the Pearl River estuary. *Continental Shelf Research*, *168*, 68–82. https://doi.org/10.1016/j.csr.2018.09.004

Laudani, R., Zhang, D., Faouzi, T., Porcu, E., Ostoja-Starzewski, M., & Chamorro, L. P. (2021). On streamwise velocity spectra models with fractal and long-memory effects. *Physics of Fluids*, *33*(3). https://doi.org/10.1063/5.0040453

Li, E., Mu, X., Zhao, G., & Gao, P. (2015). Multifractal detrended fluctuation analysis of streamflow in the Yellow River Basin, China. *Water*, *7*(4), 1670–1686. https://doi.org/10.3390/w7041670

Lortie, S. (2021). *Analysis of intermittency in turbulent flows by way of higher-order spectral moments*. McGill University (Canada).

Lortie, S., & Mydlarski, L. (2022). Investigation of internal intermittency by way of higher-order spectral moments. *Journal of Fluid Mechanics*, *932*, A20. https://doi.org/10.1017/jfm.2021.951

Lumley, J. L. (1981). Coherent structures in turbulence. In *Transition and turbulence* (pp. 215–242). Elsevier.

MacDonald, D. G., & Horner-Devine, A. R. (2008). Temporal and spatial variability of vertical salt flux in a highly stratified estuary. *Journal of Geophysical Research*, *113*(C9). https://doi.org/10.1029/2007jc004620

Malik, H., & Mishra, S. (2017). Artificial neural network and empirical mode decomposition based imbalance fault diagnosis of wind turbine using Turbsim, fast and Simulink. *IET Renewable Power Generation*, *11*(6), 889–902. https://doi.org/10.1049/iet-rpg.2015.0382

Mandelbrot, B. B., & Wallis, J. R. (1968). Noah, joseph, and operational hydrology. *Water Resources Research*, *4*(5), 909–918. https://doi.org/10.1029/wr004i005p00909

Milan, P., Wächter, M., & Peinke, J. (2013). Turbulent character of wind energy. *Physical Review Letters*, *110*(13), 138701. https://doi.org/10.1103/physrevlett.110.138701

Moegling, A. C. R. C. H., & Cochrane, G. R. (2022). Bathymetry and topography data offshore of seattle.

Movahed, M. S., Jafari, G., Ghasemi, F., Rahvar, S., & Tabar, M. R. R. (2006). Multifractal detrended fluctuation analysis of sunspot time series. *Journal of Statistical Mechanics: Theory and Experiment*, *2006*(2), P02003. https://doi.org/10.1088/1742-5468/2006/02/p02003

Nepf, H., & Geyer, W. R. (1996). Intratidal variations in stratification and mixing in the Hudson estuary. *Journal of Geophysical Research*, *101*(C5), 12079–12086. https://doi.org/10.1029/96jc00630

OES. (2023). *OES Annual Report: An overview of ocean energy activities in 2022*. International Energy Agency (IEA).

Pagnan, S., Ottonello, C., & Tacconi, G. (1994). Filtering of randomly occurring signals by kurtosis in the frequency domain. In *Proceedings of the 12th IAPR International Conference on pattern recognition, vol. 2-conference b: Computer vision & image processing* (pp. 131–133). cat. no. 94ch3440-5.

Schreiber, T., & Schmitz, A. (1996). Improved surrogate data for nonlinearity tests. *Physical Review Letters*, *77*(4), 635–638. https://doi.org/10.1103/physrevlett.77.635

Tarroja, B., Mueller, F., Eichman, J. D., Brouwer, J., & Samuelsen, S. (2011). Spatial and temporal analysis of electric wind generation intermittency and dynamics. *Renewable Energy*, *36*(12), 3424–3432. https://doi.org/10.1016/j.renene.2011.05.022

Thomson, J., Polagye, B., Durgesh, V., & Richmond, M. (2012). Measurements of turbulence at two tidal energy sites in Puget Sound, WA. *IEEE Journal of Oceanic Engineering*, *37*(3), 363–374. https://doi.org/10.1109/joe.2012.2191656

Wei, X., Schuttelaars, H. M., Williams, M. E., Brown, J. M., Thorne, P. D., & Amoudry, L. O. (2021). Unraveling interactions between asymmetric tidal turbulence, residual circulation, and salinity dynamics in short, periodically weakly stratified estuaries. *Journal of Physical Oceanography*, *51*(5), 1395–1416. https://doi.org/10.1175/jpo-d-20-0146.1

Wu, Y., He, Y., Wu, M., Lu, C., Gao, S., & Xu, Y. (2018). Multifractality and cross-correlation analysis of streamflow and sediment fluctuation at the apex of the Pearl River Delta. *Scientific Reports*, *8*(1), 16553. https://doi.org/10.1038/s41598-018-35032-z

Zhang, Q., Xu, C.-Y., Yu, Z., Liu, C.-L., & Chen, Y. D. (2009). Multifractal analysis of streamflow records of the east river basin (Pearl River), China. *Physica A: Statistical Mechanics and its Applications*, *388*(6), 927–934. https://doi.org/10.1016/j.physa.2008.11.025